JGR Space Physics

Key Points:
- Different characteristics of EPB and MSTID associated with tropical cyclones in China are analyzed in detail
- Cautions should be taken when the ROTI maps are used to identify the ionospheric irregularities since they are sensitive to both plasma bubble and MSTID
- Both EPB and MSTID show the geomagnetically conjugating feature in the East-Asia region

Correspondence to:
X. Luo and S. Gu,
xmluo@whu.edu.cn;
gsf@whu.edu.cn

Two Typical Ionospheric Irregularities Associated With the Tropical Cyclones Tembin (2012) and Hagibis (2014)

Yidong Lou[1] [iD], Xiaomin Luo[1] [iD], Shengfeng Gu[1] [iD], Chao Xiong[2] [iD], Qian Song[3] [iD], Biyan Chen[4], Qinqin Xiao[5], Dezhong Chen[1], Zheng Zhang[1], and Gang Zheng[1] [iD]

[1]GNSS Research Center, Wuhan University, Wuhan, China, [2]GFZ German Research Center for Geosciences, Potsdam, Germany, [3]Key Laboratory of Space Weather, National Center for Space Weather, China Meteorological Administration, Beijing, China, [4]School of Geosciences and Info-Physics, Central South University, Changsha, China, [5]School of Municipal and Surveying Engineering, Hunan City University, Yiyang, China

Abstract Two remarkable ionospheric irregularities named equatorial plasma bubble (EPB) and medium-scale traveling ionospheric disturbance (MSTID) are verified by using multi-instrumental observations, for example, the ground-based GPS networks, ionosonde stations, and Swarm satellites, when the tropical cyclones Tembin and Hagibis approached Hong Kong on 26 August 2012 and 15 June 2014, respectively. The low-latitude plasma bubble over an area of 105–120 °E in longitude was observed during 12:30–17:00 universal time (UT) on 26 August 2012. GPS observations from magnetically conjugate locations indicate that the nighttime bubble during 20:30–01:00 local time (LT = UT + 8h) on 26 August should be formed from the magnetically equatorial region rather than drifted from the west (eastward drift) or generated locally. Different from the EPB, during another cyclone on 15 June 2014, the northwest-southeast aligned nighttime MSTID was verified in midlatitude regions at a mean horizontal velocity of 156 m/s southwestward propagation during 12:30–17:30 UT when Hagibis was near the mainland coast. By comparing the ionospheric observations during the two cyclones, differences are identified: small-scale irregularities associated with plasma bubble cause obvious perturbations of the rate of total electron content index with the value of ~3.0 TECU/min; while the MSTID in midlatitude only cause relatively slight rate of total electron content index disturbances with the value of ~1.5 TECU/min. In addition, the magnetic conjugacy of EPB and MSTID in two hemispheres during the passage of tropical cyclones has been also discussed in this study.

1. Introduction

Tropical cyclone is a rapidly rotating storm system characterized by a low-pressure cyclonic vortex at the center of a region with mesoscale convection (Rivoire et al., 2016). Depending on its location and strength, a tropical cyclone is referred to by different names such as hurricane, typhoon, tropical storm, and tropical depression. In the Asia-Pacific region, the tropical cyclones are generally divided into three stages according to the maximum sustained wind speeds (v_{max}), namely, tropical depressions ($v_{max} < 17$ m/s), tropical storms (17 m/s $\leq v_{max} < 33$ m/s), and typhoons ($v_{max} \geq 33$ m/s; e.g., Kim et al., 2010). During the lifetime of tropical cyclone, the propagation of acoustic-gravity waves (AGWs; Kim & Chun, 2011) and the arising electric fields (Sorokin et al., 2005) are often observed, which have the possibility to induce traveling ionospheric disturbances (TIDs) or plasma bubbles (e.g., Isaev et al., 2010). Statistical results of Xiao et al. (2007) indicated that TIDs were detected in 92% of their typhoon cases (22 vs. 24) from 1987 to 1992 in mainland China. To global navigation satellite system (GNSS) users, severe ionospheric irregularities can degrade the accuracy of GNSS measurements, thus affecting high-precision applications (Hernández-Pajares et al., 2006; Lejeune et al., 2012; Luo et al., 2018).

Over the past years, the ionospheric irregularities associated with tropical cyclones have been reported by many studies, which can be summarized as two focuses in general, that is, the morphological characteristics (e.g., Chou et al., 2017; Song et al., 2017; Xiao et al., 2007) and the physical mechanism (e.g., Ke et al., 2018; Sorokin et al., 2005). For the former topic, Xiao et al. (2007) pointed out that during the lifecycle of typical cyclone, most TIDs are the linear medium-scale TIDs (MSTIDs), which generally have speeds of 100–250 m/s and wavelengths of several hundred kilometers with periods of 2–5, 10–20, and over 20 min (Polyakova & Perevalova, 2011). Previous studies also indicated that the amplitude of the MSTIDs can

reach ~2 TECU (Kong et al., 2017; Song et al., 2017), which represents a range error of about 0.32 and 0.54 m in GPS L1 and L2 measurements, respectively. Generally, the structures of TIDs triggered by tropical cyclones are the nearly linear forms, but recently the concentric TIDs were also reported when the super typhoon Meranti was approaching Taiwan on 13 September 2016 (Chou et al., 2017). It provided new evidences of typhoon-induced concentric gravity waves in the ionosphere. Due to the complexity of the tropical cyclone, the influence of the tropical cyclone-ionosphere on the atmosphere is still not clarified. The AGW generated by the tropical cyclone is considered as one mechanism source of the ionospheric disturbance occurrence (Huang et al., 1985; Kim & Chun, 2011). However, some analyses revealed that no obvious statistical correlation can be found between the cyclone driven AGWs and ionospheric disturbances (Zakharov & Kunitsyn, 2012). For example, the 2–4 hr duration of ionospheric disturbances caused by four typhoons in Australia during 2005–2014 did not match well with those caused by AGWs with a few minutes to 3-hr duration (Li et al., 2018). Some studies pointed out that the coupling mechanism such as electric fields, neutral winds, and the turbulent layer movements might be used to explain the interaction of ionosphere associated with tropical cyclones (Ke et al., 2018; Sorokin et al., 2005).

Except the TIDs, very few studies reported plasma bubbles and related ionospheric scintillations during tropical cyclones (e.g., Ke et al., 2019; Yang & Liu, 2016a). It is well acknowledged that ionospheric scintillation is the signal diffractive effects in nature (Kintner et al., 2007). The condition of scintillation occurrence is that the radio signal should propagate several small-scale irregularities near the first Fresnel length (e.g., ~400 m for the GPS L1 signal), thus resulting in signal amplitude and phase fluctuations. However, the scale of TIDs triggered by tropical cyclones is generally several hundred or even thousands of kilometers, they usually cause the small magnitude fluctuations of the total electron content (TEC; 1–2 TECU), thus rarely resulting in scintillation of GNSS signals. Although several evidences supported the gravity wave seeding of ionospheric irregularities and scintillations (Fritts et al., 2008; Lay, 2018; Taori et al., 2011), the relationship between tropical cyclone and ionospheric scintillation is still unclear. Yang and Liu (2016a) for the first time reported the strong scintillation phenomenon associated with the 2012 tropical cyclone Tembin passed closely to Hong Kong. They suspected that gravity waves might be generated by the Tembin and resulting in plasma irregularities occurrence on 26 August 2012. Due to the limited observations coverage such as those from the ionospheric scintillation monitor receivers (ISMRs) and space-based GPS receivers, it is hard to determine whether the ionospheric irregularities were generated locally or drifted from adjacent area. In addition, the plasma bubble reported by Yang and Liu (2016a) is observed at the equatorial ionization anomaly (EIA) within $\pm15°$ magnetic latitudes (MLAT), where is the place with frequent occurrence of equatorial plasma bubbles (EPBs) and ionospheric scintillations (Appleton, 1946; Kelley, 2009; Lin et al., 2007). Therefore, further work is still needed to investigate the ionospheric irregularities occurred on 26 August 2012 during the passage of Tembin.

This study presents a comprehensive investigation of the plasma bubble responding to the tropical cyclone Tembin in 2012 using the multi-instrumental observations from 205 GPS stations, four magnetically conjugate GPS stations, as well as one ionosonde station. Moreover, another typical case of ionospheric irregularity as MSTID associated with the tropical cyclone Hagibis in 2014 is also analyzed in detail. As far as we know, there has been no comparison of the MSTID and plasma bubble related to tropical cyclones in China. This paper is structured as follows. The data and method used to study the tropical cyclones Tembin and Hagibis are described first. Thereafter, we present the detailed results, analysis, and discussions for the two typical ionospheric irregularities responding to the tropical cyclones. Finally, the summary is given in the last section.

2. Data and Method

According to the Tropical Cyclone Annual Publication of Hong Kong Observatory in 2012 (Hong Kong Observatory, 2012), Tembin formed as a tropical depression over the western North Pacific about 660-km northeast of Manila on 18 August 2012 as shown in Figure 1. The red dotted line represents the trajectory of Tembin. It passed close to Taiwan twice on 24 and 28 August, respectively. On 25 August, Tembin was closest to Hong Kong (~290 km) at around 17 universal time (UT). It weakened into a tropical storm on 30 August. Another tropical cyclone Hagibis (blue dotted line in Figure 1) formed as a tropical depression over the northeastern part of the South China Sea on the morning of 14 June 2014 (Hong Kong
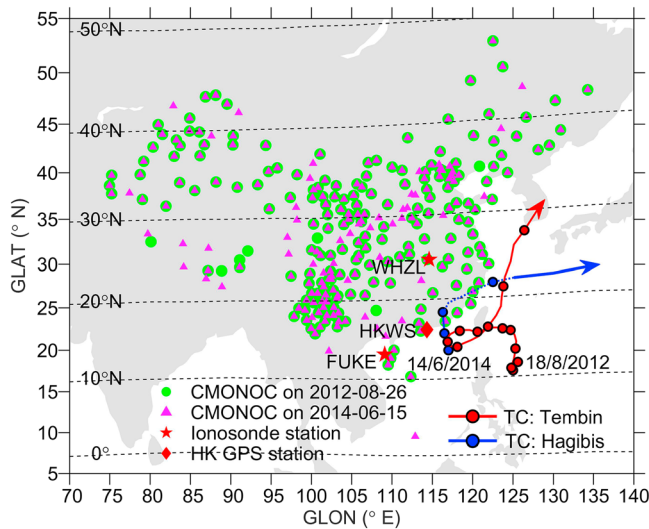
Figure 1. The trajectory of tropical cyclone Tembin during 18–30 August 2012 (red dots) and Hagibis during 14–17 June 2014 (blue dots). The blue or red dots represent the location of tropical cyclone at 00:00 UT on each day. The green circles and magenta triangles indicate the location of Crustal Movement Observation Network of China stations on 26 August 2012 and 15 June 2014, respectively. The red pentagrams represent the location of ionosonde stations FUKE and WHZL. The red diamond represents the location of HKWS station in Hong Kong. The black dashed lines represent the magnetic latitudes.

Observatory, 2014). It intensified into a tropical storm on the afternoon and reached its peak intensity on the night of 14 June 2014. On 15 June, it moved steadily northward and weakened into a tropical depression during the night. Hagibis further weakened on June 16, but it reintensified into a tropical depression on the afternoon of 17 June and finally evolved into an extratropical cyclone on 18 June. As shown in Figure 1, Hagibis was closest to Hong Kong with ~260 km at 1:00 UT on 15 June. Reported by the Hong Kong Observatory (2012, 2014), the average central pressure of two cyclones are comparable (~990 vs. ~960 hPa), but the average wind force of Tembin (~35 m/s) is larger than that of Hagibis (~15 m/s). In addition, the Tembin did not land in mainland China, while the Hagibis edged toward the coastal areas of eastern Guangdong on 15 June and made landfall near Shantou on that afternoon.

To sufficiently investigate the ionospheric irregularities induced by tropical cyclones, multi-instrumental data are used in this study and the geographical distributions of these stations are depicted in Figure 1. Specifically, dual-frequency GPS data collected at more than two hundred GPS stations (205 stations in 2012 marked by the green circles and 245 stations in 2014 marked by the magenta triangles) supported by the Crustal Movement Observation Network of China are used. GPS station HKWS (red diamond) managed by the Lands Department of Government of Hong Kong Special Administrative Region is also used to fill the data vacancy in Hong Kong. In addition, the ionograms derived from two ionosonde stations FUKE and WHZL marked by the red pentagrams in Figure 1 are utilized to verify the spread-F during the passages of Tembin and Hagibis. In the data processing, all ground-based GPS observations with the sampling interval of 30 s are used to calculate the rate of total electron content index (ROTI). To reduce the effects of nonirregularities related tracking errors such as multipath, only the GPS data observed above 30° elevation angle are considered. Except the ground-based observations, the space-based in situ electron density (0.5-s sampling rate) and GPS measurements (1-s sampling rate) from Swarm A and C during the passage of Hagibis on 15 June 2014 are also used for the cross validation of ionospheric irregularities.

The ROTI is defined as the standard deviation of rate of TEC with a sliding window for each 5-min interval (Pi et al., 1997):

$$ROTI = \sqrt{\langle ROT^2 \rangle - \langle ROT \rangle^2} \qquad (1)$$

The ROT at epoch (k) can be calculated by the differencing TEC for each sampling interval:

$$ROT = \frac{TEC(k) - TEC(k-1)}{\Delta t} \qquad (2)$$

where TEC, in a unit of TECU (1 TECU = 10^{16} el/m^2), at the epoch (k) can be estimated with high precision from a geometric-free combination of the carrier phase measurements. For the ground-based GPS data, we apply a threshold of ROTI larger than 0.5 TECU/min together with a condition of multipeak detection algorithm for identifying the ionospheric perturbations (Luo et al., 2018).

3. Results and Analysis

3.1. ROTI Responding to Ionospheric Irregularities

Figure 2 presents the time series of ROTI derived from HKWS station (22°26′N, 114°20′E; geomagnetic latitude: 15°48′N) during the lifetime of tropical cyclones Tembin and Hagibis. HKWS is located at the east of Hong Kong and is very close to the passage of Tembin on 26 August 2012 and Hagibis on 15 June 2014. Figure 2 also gives the corresponding solar F10.7, geomagnetic Kp and Dst information. As shown in
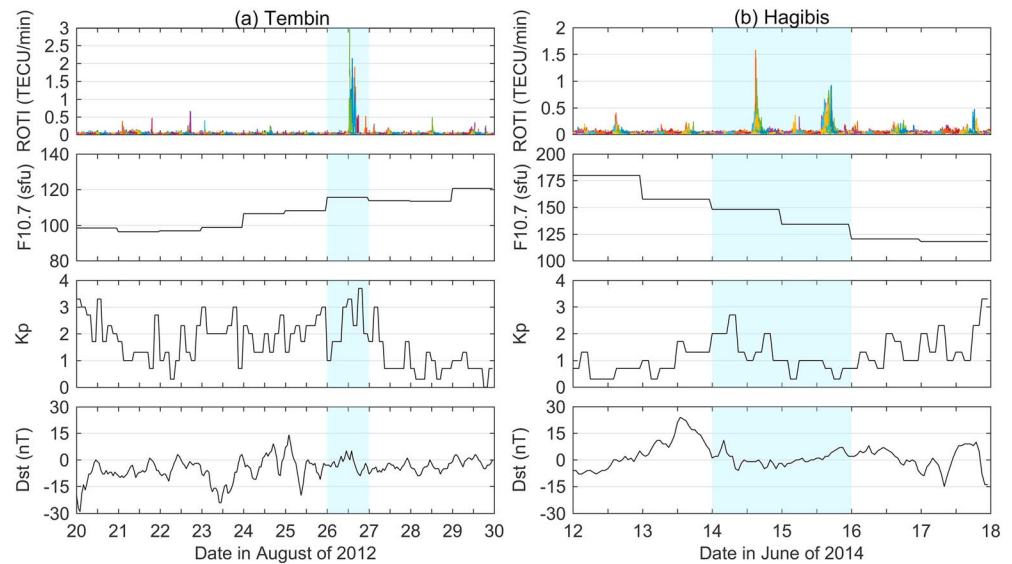
Figure 2. Time series of ROTI for all GPS satellites and the corresponding *F*10.7, Kp, and Dst indexes during 20–30 August 2012 and 12–18 June 2014. The time periods of ionospheric perturbations are highlighted in blue. Note that the time shown in the *x* axis is based on UT system. ROTI = rate of total electron content index; TECU = total electron content unit.

Figure 2a, an obvious enhancement of ROTI can be observed on 26 August 2012 when the Tembin approached to Hong Kong (~300 km), while no significant increase was observed on other days. On 26 August, the maximum ROTI can reach ~3.0 TECU/min, but the ROTI values on other days were generally smaller than 0.2 TECU/min. Similar results were also observed by the dedicated ISMR installed at Hong Kong (Yang & Liu, 2016a). In Figure 2b, a significant variation of ROTI can be seen on 14 and 15 June 2014 when the Hagibis was passing Hong Kong, but for other days, the time series of ROTI were generally stable (~0.2 TECU/min). From the panels of *F*10.7, Kp, and Dst indexes, we can find that the solar activity (*F*10.7 < 150 sfu) and geomagnetic activity (Kp < 4; −30 nT < Dst < 30 nT) are stable during the lifetimes of Tembin and Hagibis. Without significant solar flare and geomagnetic storm activities, it is suggested that the remarkable enhancements of ROTI might be associated with the tropical cyclones. On the other hand, we can note that the magnitudes of ROTI enhancements in Tembin are generally larger than those of in Hagibis, suggesting that the ionospheric irregularities responding to two cyclones might be different.

Figure 3 shows the spatial distributions of ROTI for each affected GPS satellite (ROTI > 0.5 TECU/min) observed by HKWS on 26 August 2012 and 15 June 2014. The results of ROTI on 14 June 2014 are not shown here since they were similar to those on 15 June 2014 (same as below). The trajectories of GPS satellites with different pseudo random noise (PRN) are represented by the ionospheric pierce points (IPPs) mapped onto an altitude of 450 km. The time periods of affected satellites and trajectories of Tembin and Hagibis are also presented in the right bottom corner of Figure 3. As shown in Figure 3a, we can clearly find that larger values of ROTI (>0.5 TECU/min) were located at the southward of HKWS (10°–15° MLAT), which was rightly situated in the EIA region (±15° MLAT) with the frequent EPBs occurrence. Meanwhile, GPS satellites (PRNs G9, G15, G21, G26, G27, and G29) experienced large ROTI were rightly during 12:30–18:00 UT (20:30–2:00 LT) when strong nighttime EPBs and scintillations occurred. From the above two points, it is reasonable to deduce that the large ROTI values should be attributed to the nighttime plasma bubbles. The detailed analyses of the origin of plasma bubbles are shown next. From Figure 3b, IPPs with larger ROTI values on 15 June 2014 were located at the northward of HKWS (18°–22° MLAT) and their magnitude was around 0.6 TECU/min, which is far smaller than those ROTI values on 26 August 2012. Meanwhile, the trajectories of IPPs with large ROTI values were rightly over the path of Hagibis except G29. The time period of G29 experienced ionospheric perturbations was during 16:50–17:20 UT, which is far later than that of other satellites, so we think that the west irregularities might be shifted from the east region. The detailed spatial distributions of the ionospheric irregularities associated with the two tropical cyclones will be shown below.
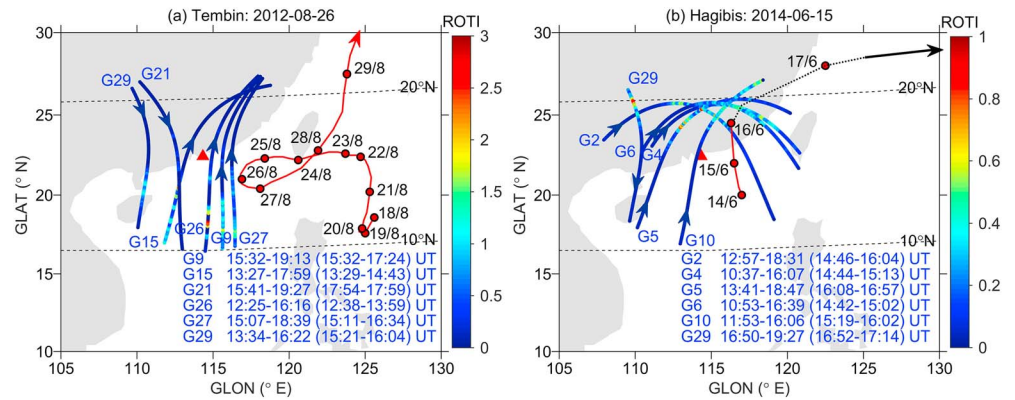
Figure 3. The ROTI along the trajectories of GPS satellites experienced ionospheric perturbations on 26 August 2012 and on 15 June 2014. The time period of each satellite tracked by HKWS is shown at the right bottom corner and that in the parentheses indicates when ROTI larger than 0.5 TECU/min.

3.2. Equatorial Plasma Bubbles During the Passage of Tropical Cyclone Tembin

Figure 4 shows two-dimensional ROTI maps derived from 205 Crustal Movement Observation Network of China stations during the period of 12:15–17:45 UT on 26 August 2012, when the tropical cyclone Tembin was ~300km to Hong Kong. The ROTI values are averaged in 1° × 1°. At 12:15 UT, all the ROTIs were smaller than 0.3 TECU/min, indicating no ionospheric irregularity at this time (Figure 4a). The irregularities were formed in the southeast region at around 12:45 UT and then they reached a strong level until 13:45 UT with few ROTIs larger than 1.0 TECU/min (Figure 4d). After that, the irregularities weakened at around 14:15 UT (Figure 4e) and intensified again at 15:45 UT (Figure 4h). Two hours later, the ionosphere got quiet
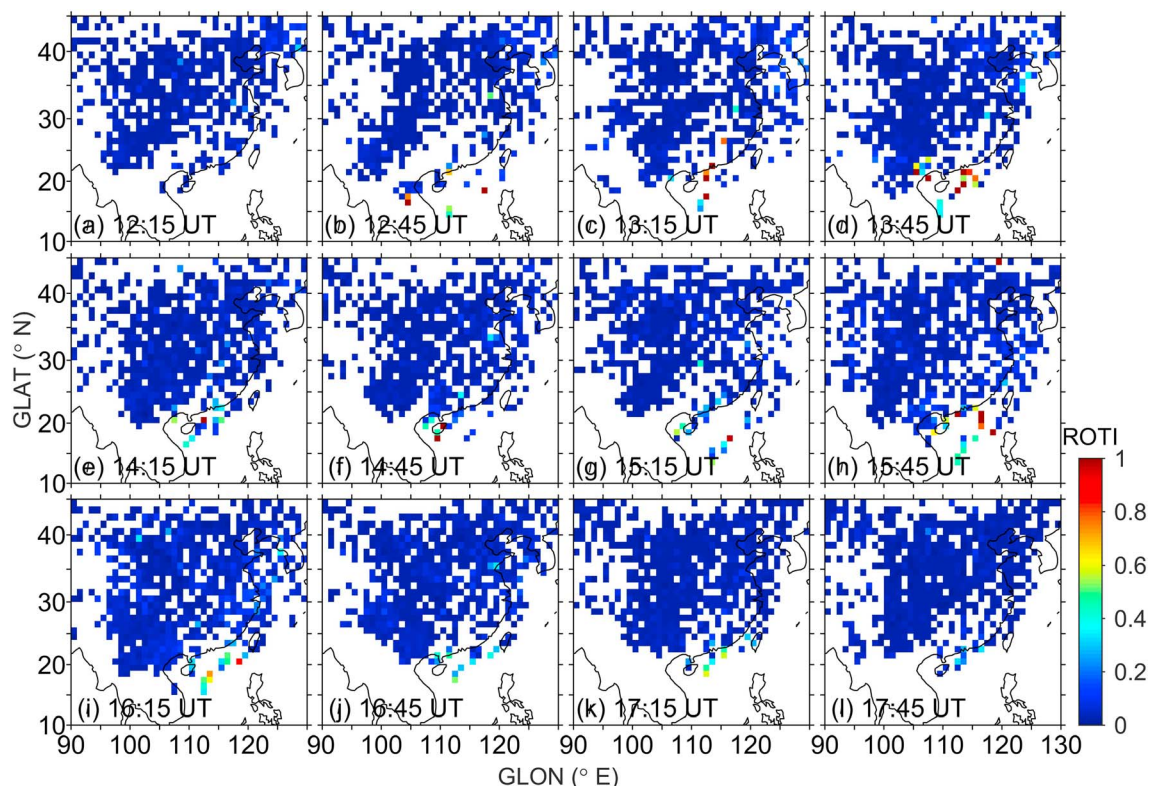

Figure 4. Two-dimensional of ROTI maps during the period of 12:15–17:45 UT (a–l) on 26 August 2012 when the tropical cyclone Tembin passed through Hong Kong.
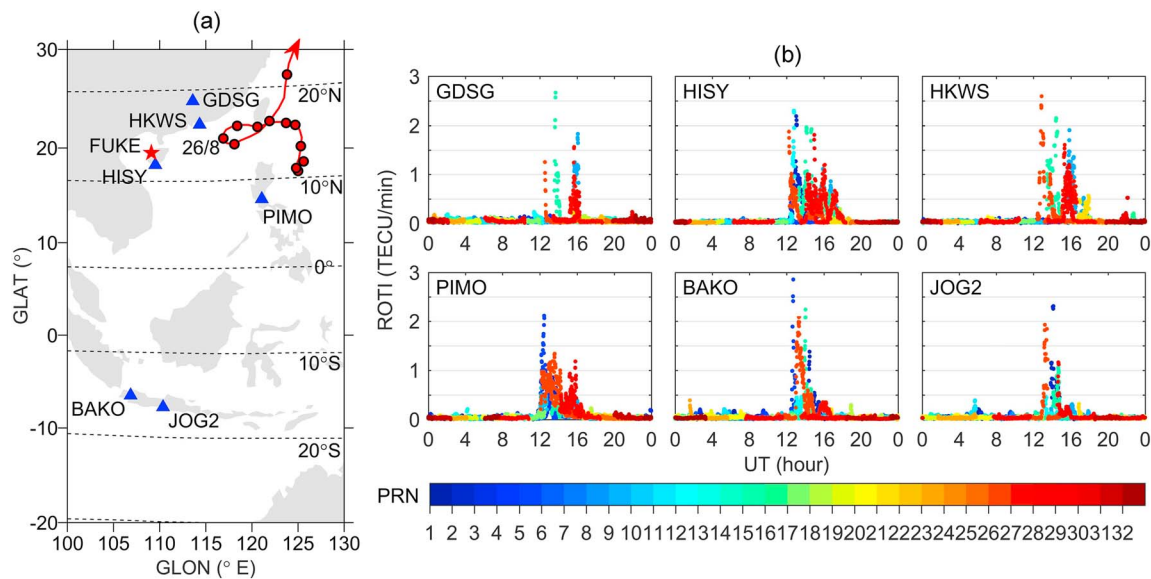
Figure 5. Geographical distribution of six GPS stations (triangle) and one ionosonde station (pentagram) used to confirm the ionospheric perturbations during the passage of tropical cyclone Tembin on 26 August 2012 (a) and the corresponding variations of ROTI for the six stations (b). PRN = pseudo random noise; ROTI = rate of total electron content index; TECU = total electron content unit.

again (Figure 4l). From the panels, the magnitude of perturbations had an obvious variation from 0.1 to 1.0 TECU/min during 12:15–17:45 UT, but it is hard to see their drift state. In addition, the scale of irregularities covered an area within 15–22 °N and 105–120 °E. We suspected that the irregularities belong to EPBs in Figure 4. Under this hypothesis, they should be generated at the equatorial *F* region first and then elongated along the magnetic flux tubes with $\pm 20°$ MLAT (e.g., Kelley, 2009). To verify the assumption, we therefore further check the observations from the magnetically conjugate stations as well as the ionosonde station.

Figure 5 presents the geographical distribution of six GPS stations and the corresponding variations of ROTI on 26 August 2012. The stations HISY and BAKO, as well as HKWS and JOG2, are the near magnetically conjugate stations as shown in Figure 5a. It is clearly seen that significant variations of ROTI were observed at the conjugate stations (HISY vs. BAKO; HKWS vs. JOG2) in both hemispheres, indicating that the ionospheric irregularities during the passage of Tembin on 26 August 2012 are the EPBs instead of the local plasma bubbles. From the west to east direction (HISY-PIMO; BAKO-JOG2), the onset time of perturbations (ROTI > 0.5 TECU/min) were almost the same (around 12:30 UT), suggesting that EPBs should not be drifted from other area. In addition, the ROTIs for the GDSG in the north (~20° MLAT) and JOG2 in the south (~−20° MLAT) also showed obvious variations during the nighttime period (12:30−17:00 UT), which is also consistent with the latitude scale of EPBs as mentioned before. Note that the magnitude of ROTIs for the northern stations presented in Figure 5b experienced a weak (12:30, 14:00, and 17:00 UT) to strong (13:30 and 16:00 UT) progress. The above analyses show good consistency to the ROTI maps shown in Figure 4.

Except GPS observations, the ionosonde data collected at FUKE station (19°31′N, 109°08′E; geomagnetic latitude: 12°49′N) in Hainan province (red pentagram in Figure 5a) were also used to verify the EPBs during the passage of Tembin on 26 August 2012. Four samples of ionograms from the ionosonde were plotted in Figure 6. Strong range-type spread-*F* (a signature of EPBs in ionograms) was observed around 300- to 500-km altitude at 12:45, 13:45, 14:45, and 15:45 UT, with durations of about 5 hr until 17:00 UT on 26 August. From the above analyses, we can conclude that the ionospheric irregularities responding to Tembin are EPBs, which are not drifted from the west nor generated locally.

3.3. Medium-Scale Traveling Ionospheric Disturbances During the Passage of Tropical Cyclone Hagibis

Figure 7 shows the ROTI maps observed during 12:00–17:30 UT on 15 June 2014 when the tropical cyclone Hagibis was close to Guangdong province. The ionospheric irregularities originally formed in the northeast of China on 12:30 UT (Figure 7b) with the value of ~0.4 TECU/min and then their scale was increasing
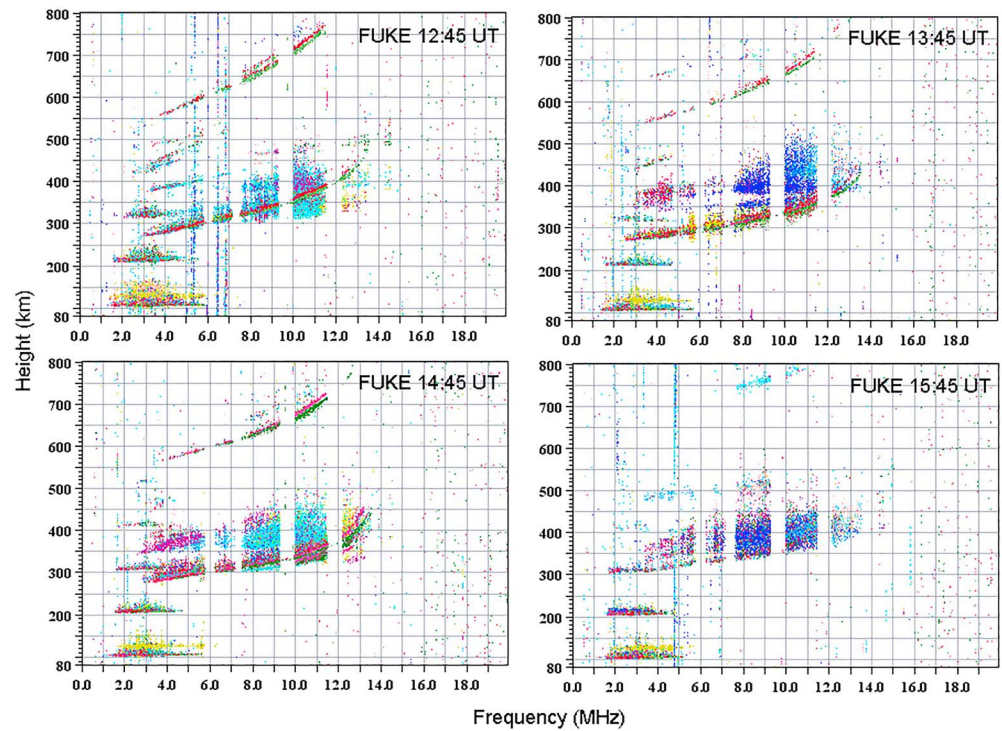
Figure 6. Ionograms showing the presence of EPBs over FUKE station in Hainan province at 12:45, 13:45, 14:45, and 15:45 UT on 26 August 2012.
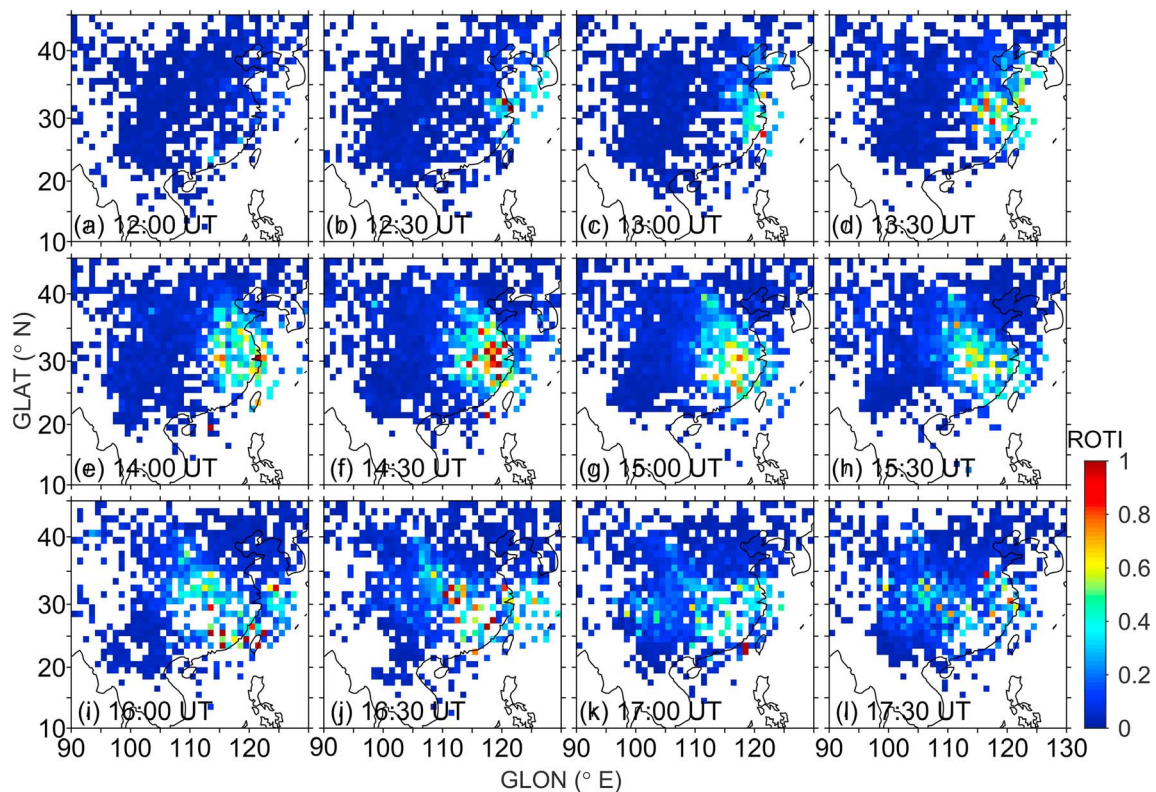

Figure 7. Two-dimensional of ROTI maps during the period of 12:00–17:30 UT (a–l) on 15 June 2014 when the tropical cyclone Hagibis passed through Hong Kong. ROTI = rate of total electron content index.
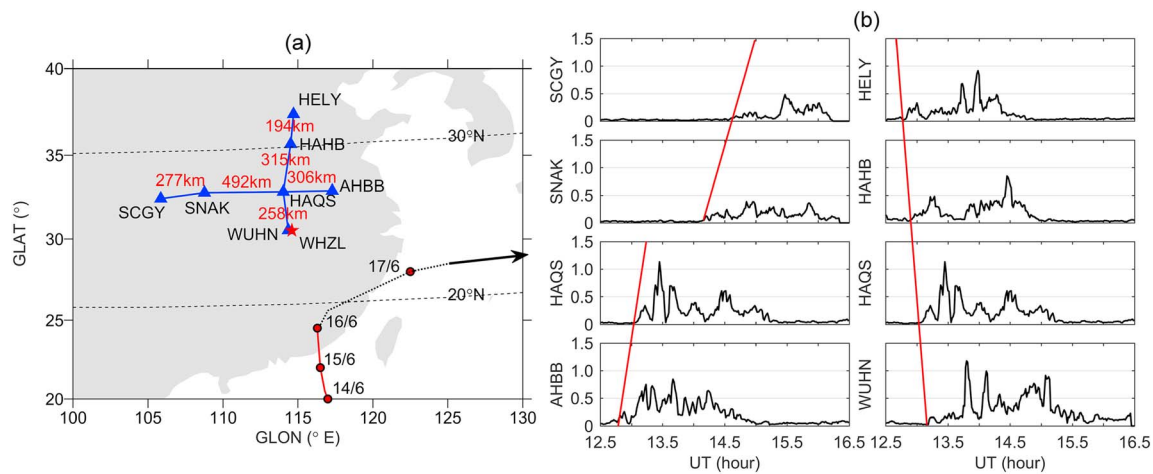
Figure 8. Geographical distribution of seven GPS stations (blue triangle) and one ionosonde station (red pentagram) used to confirm the ionospheric perturbations during the passage of tropical cyclone Hagibis on 15 June 2014 (a) and the corresponding variations of rate of total electron content index of PRN G10 for the seven stations (b).

gradually until around 16:30 UT (Figure 7j) but showed a southwestward propagation. During the period of time, the maximum horizontal extension and the amplitude of the perturbations were about 900 km and 1 TECU/min. Compared to the results in Figure 4, the scale of ionospheric irregularities shown in Figure 7 was much larger and they were located at the midlatitude regions.

Figure 8 presents the ROTI observations of PRN G10 observed simultaneously by seven GPS stations with the west to east and north to south distribution. In addition, four samples of ionograms from the ionosonde station WHZL (30°31′N, 114°36′E; geomagnetic latitude: 24°30′N), which is rightly located in the perturbation region (see Figure 8a), are also depicted in Figure 9. From Figure 8b, it is easily found that the stations in
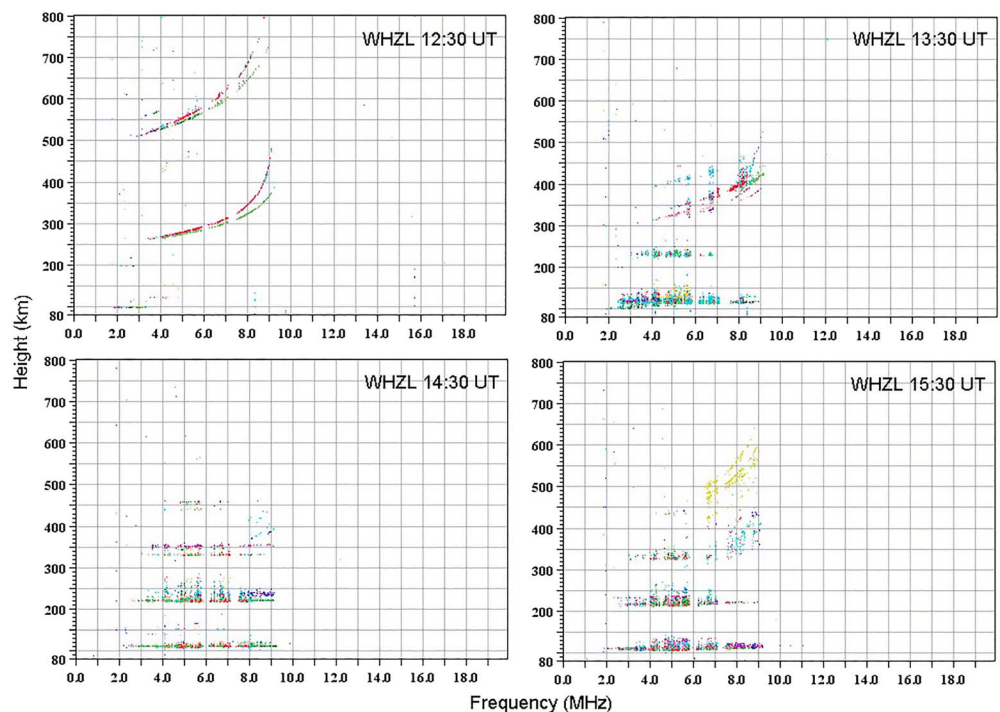

Figure 9. Ionograms showing the absence of EPBs over station WHZL in Hubei province at 12:30, 13:30, 14:30, and 15:30 UT on 15 June 2014.
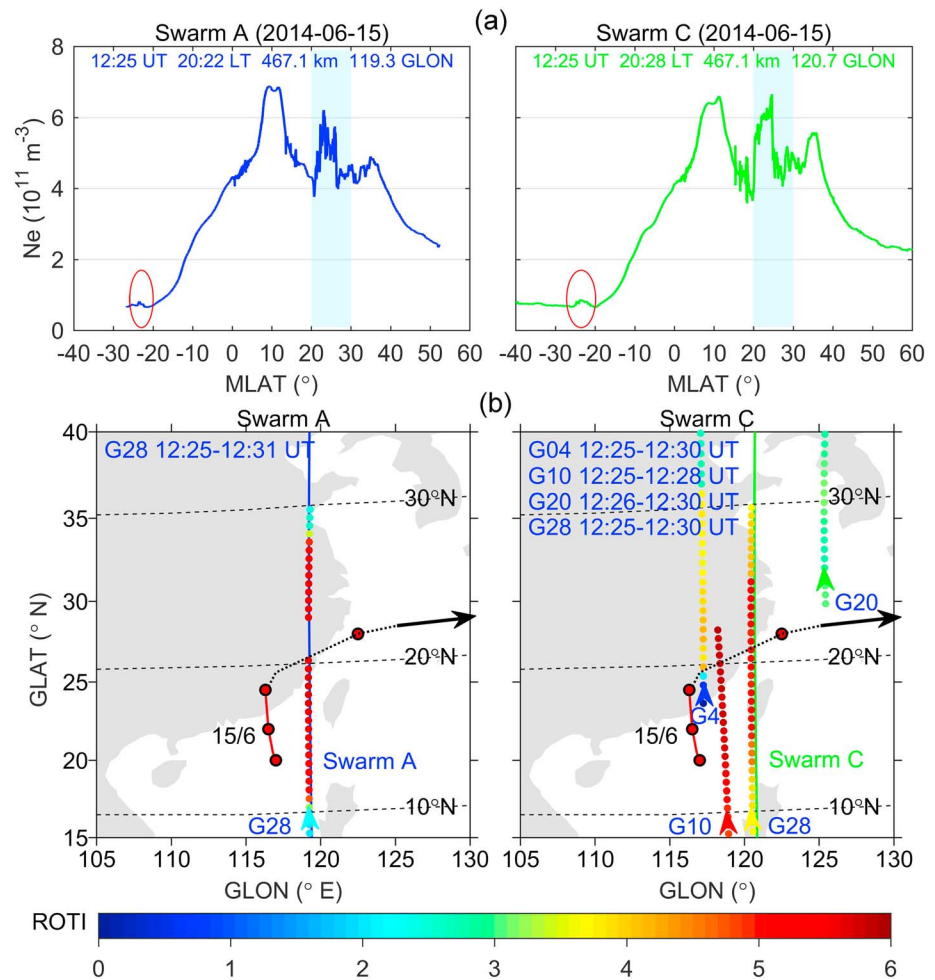
Figure 10. (a) Time series of in situ electron density from Swarm A (blue) and C (green) when they passed through China longitude (~120 °E) on 15 June 2014. (b) The ROTI along the trajectories of GPS satellites tracked by the onboard receiver of Swarm A and C. ROTI = rate of total electron content index.

the east (north) experienced earlier ionospheric perturbations than those located in the west (south), further indicating the southwestward propagation characteristic of ionospheric irregularities. Based on the distance and time delay for different stations, the horizontal propagation velocity of 159 (SCGY-SNAK), 132 (SNAK-HAQS), and 176 m/s (HAQS-AHBB) for the irregularities were calculated. The mean horizontal velocity is 156 m/s, showing a good agreement with the value of 132 m/s for the MSTID trigged by the typhoon Matmo on 23 July 2014 in China region (Song et al., 2017). Considering the propagation direction (southwestward) and occurrence region (20°–30° MLAT), the ionospheric irregularities observed on 15 June 2014 should be the MSTID instead of plasma bubbles. The ionograms shown in Figure 9 further suggest that no obvious plasma bubbles were observed over the WHZL during the period of 12:30–15:30 UT although obvious ionospheric irregularities appeared around it (see the ROTI variation of WUHN station in Figure 8b). Interestingly, the "weak spread-F" can also be seen around 400 km in the ionograms at 13:30 and 15:30 UT, which means that the nighttime $F2$ region irregularities have the possibility to accompany with the MSTID occurrence in the midlatitude.

On 15 June 2014, the Swarm A and C passed through the longitude of ~120 °E at around 12:30 UT. The in situ electron density (Ne) measurements and onboard GPS data from Swarm satellites can provide a good cross validation of MSTID. The time series of Ne and trajectories of ROTI IPPs for each affected GPS satellite (ROTI > 3 TECU/min) observed by Swarm A and C are shown in Figure 10. The UT, LT, altitude, and geographic longitude (GLON) when Swarm low pair satellites passed near Hagibis at 12:25 UT on June 15
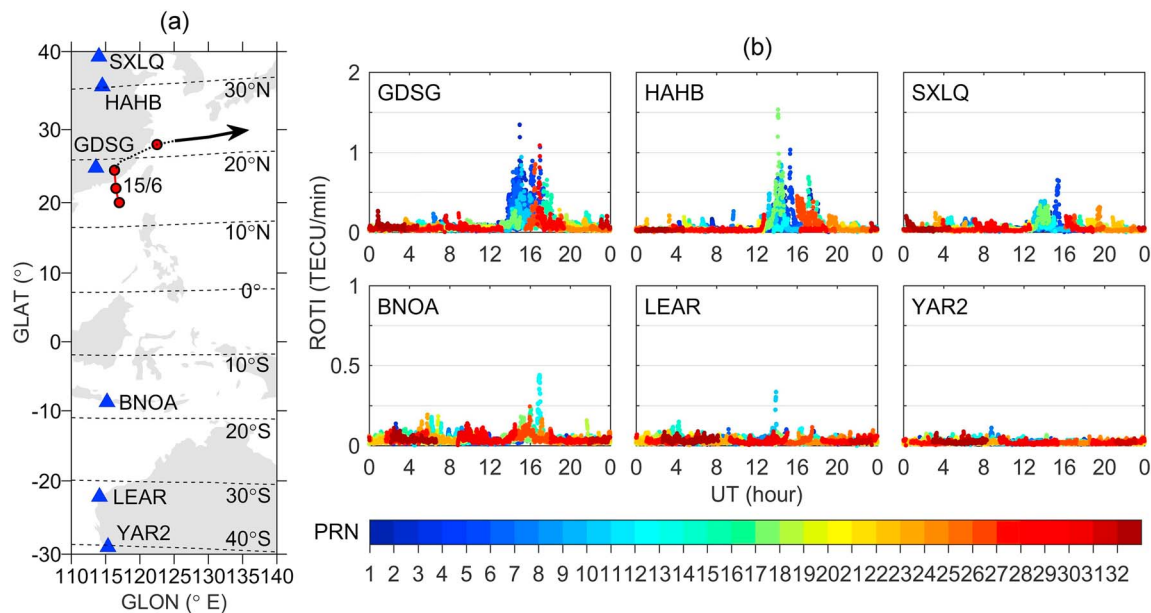
Figure 11. Geographical distribution of six GPS stations (triangle) used to confirm the MSTID conjugacy during the passage of tropical cyclone Hagibis on 15 June 2014 (a) and the corresponding variations of ROTI for the six stations (b). PRN = pseudo random noise; ROTI = rate of total electron content index; TECU = total electron content unit.

(~22 °N) are listed at the topside of the figure. Since at 12:25 UT Swarm A and C were located at 119.3° and 120.7° GLON, respectively, 6-min difference in LT can be seen in the figure. Similar to Zakharenkova et al. (2016), we applied a threshold of ROTI larger than 3 TECU/min for the space-based GPS data to identify the ionospheric perturbations under quiet geomagnetic conditions. Note that a threshold of 0.5 TECU/min has been used for the ground-based GPS data. Due to the relatively low speed of GPS satellite with respect to a ground-based station, the ROTI derived from ground-based receiver mainly reflects the movement of ionospheric irregularity, while the ROTI derived from spaceborne receiver reflects more the irregularity structure along the low Earth orbit satellite track, like Swarm, due to the high speed of low Earth orbit satellite (Luo et al., 2019). As shown in Figure 10a, at around 12:30 UT Swarm Ne measurements experienced an abrupt increase (~2 × 10^{11} m^{-3}) at the 20° MLAT and then fluctuated slightly until 28° MLAT (see the blue region). The ROTI IPPs shown in Figure 10b also indicate several GPS satellites signal encountered ionospheric irregularities at the region of 20°–30° MLAT. The above results show a good consistency to the MSTID region as shown in Figure 7b. In addition, it should be noted that in 10°–20° MLAT the PRNs G28 and G10 also showed larger ROTI around 6 TECU/min. This should be attributed to the fluctuation of Ne in the northern EIA (see the variations of Ne in 10°–20° MLAT region in Figure 10a). For the Southern Hemisphere, it is interesting to see a slight increase in Ne shown in -25°–-22° MLAT region (red cycle), which might imply the MSTID also mapped into the opposite hemisphere.

To further verify the MSTID conjugacy, Figure 11 presents the ROTI variations from six near conjugate stations (GDSG vs. BNOA; HAHB vs. LEAR; SXLQ vs. YAR2) on 15 June 2014. From the top panels of Figure 11b, obvious fluctuations of ROTI for the northern stations can be seen during 12:30–17:30 UT. Since the location of SXLQ is at around 40 °N near the edge of MSTID, the corresponding ROTI showed a small variation around 0.5 TECU/min during 12:30-17:30 UT. Compared to the Northern Hemisphere, the time series of ROTI derived from southern stations were relatively stable, but few satellites for stations BNOA and LEAR still encountered ionospheric perturbations around 16:00 UT. For example, the ROTI of PRN G12 derived from BNOA can reach ~0.5 TECU/min at 16:40 UT. Since the background electron density in the Southern Hemisphere is very small (~0.8 × 10^{11} m^{-3}) as shown in Figure 10a, the perturbation reflected in ROTI is unremarkable. From the above analysis, we can find that the midlatitude nighttime MSTID also has the feature of magnetic conjugacy but show different magnitude of Ne and ROTI values between two hemispheres.

4. Discussions

Two typical ionospheric irregularities as the plasma bubble and MSTID associated with tropical cyclones are detailed analyzed in this study. The former one was revealed by Yang and Liu (2016a) using the dedicated ISMR measurements, but they did not investigate the origin of the bubble due to the limited observation coverage. Using GPS and ionosonde measurements, we further verify that the plasma bubble associated with Tembin is neither drifted from its west nor formed locally but initiated from the magnetically equatorial region. The EPBs are known to be generated at low latitudes around the magnetic equator through the generalized Rayleigh-Taylor instability mechanism (e.g., Kelley, 2009). Because of the unstable density perturbations of rapidly rising F layer, the large depleted density irregularities can expand along the magnetic field lines to F region heights over latitudes off the equator within $\pm 20°$ MLAT (e.g., Abdu et al., 2009; de Paula et al., 2010). The initial "seed" of the unstable density perturbations is widely considered as gravity waves (e.g., Huang & Kelley, 1996; Singh et al., 1997; Takahashi et al., 2009). Huang and Kelley (1996) pointed out that the gravity waves initiate the Rayleigh-Taylor instability via spatial resonance, then the instability grows and amplifies the perturbations induced by gravity waves and possibly induce plasma bubbles in final. The observational evidences of gravity waves initiation of ionospheric plasma bubbles have been shown in several studies based on the data from spread F Experiment (SpreadFEx) in Brazil (Abdu et al., 2009; Fritts et al., 2008; Takahashi et al., 2009).

The plasma bubble with longitude scale of 105–120 °E shown in Figure 4 was observed on 26 August 2012 during the passage of Tembin. Under the normal solar and geomagnetic conditions on this day, Yang and Liu (2016a) suspected that the gravity waves might be generated in the lower atmosphere and contributed to the tropical cyclone-ionosphere interaction. Many previous studies suggested that the tropical cyclone is the possible sources of gravity waves since the former one is a well-organized and vigorous convective system, and the convective "cells" in the eyewall and spiral bands can induce the gravity waves via mechanical oscillator effect, deep heating, or obstacle effect (e.g., Dhaka et al., 2003; Kim et al., 2009; Kim & Chun, 2005). If the plasma bubble responding to Tembin is triggered by the gravity wave, which implies this gravity wave should be propagated from the tropical cyclone eye (14.3° MLAT at 0:00 UT on 26 August) to the magnetic equator (~1,500 km) first and then seeded the initial instability. However, due to lack of gravity wave observations, the above hypothesis could not be verified in the present study.

The MSTID associated with tropical cyclone Hagibis shown in Figure 7 went along a northwest-southeast alignment and propagated southwest direction with a mean velocity of 156 m/s. This is consistent with the nighttime MSTIDs characteristics in the Northern Hemisphere (e.g., Saito et al., 1998; Song et al., 2017; Tsugawa et al., 2007). Meanwhile, the MSTID was observed on 15 June 2014 when the Hagibis was to land the mainland coast, which is also in agreement with the previous studies (e.g., Kong et al., 2017; Xiao et al., 2007). Because of the large energy released by tropical cyclones during the landing phase, the gravity waves might be excited by the rapid loss of momentum and viscous interactions. As mentioned before, the gravity waves can propagate to the ionosphere altitude and disturb the ionospheric electron density, thus triggering the MSTID occurrence. Another feature of the MSTID is its conjugacy as shown in Figures 10 and 11, but the ROTIs are quite different in the two hemispheres. This difference should be contributed to the discrepancy in the background electron density of two hemispheres as shown in Figure 10a (5.0×10^{11} m^{-3} in the north vs. 0.8×10^{11} m^{-3} in the south). The 10-year (1996–2005) ion density measurements from the Defense Meteorological Satellite Program spacecraft indicated that the ion density with maxima around June solstice in the Northern Hemisphere and December solstice in the Southern Hemisphere (Liu et al., 2007). The MSTID shown in this study occurred on 15 June 2014, which is during summer solstice in the Northern Hemisphere when the Sun's zenith is at the tropic of cancer (23.5 °N), so the discrepancies of Ne and ROTI between two hemispheres are likely caused by the seasonal influence on the background ionosphere. In addition, the lower ROTIs in the Southern Hemisphere match well with the airglow intensities obtained by all-sky imager at Darwin (12.4 °S, 131.0 °E) in Figure 9 of Shiokawa et al. (2005) and TEC perturbations values measured in south America in Figure 4 of Valladares and Sheehan (2016).

Another interesting finding in this study is that the values of ROTI maps reflected in the EPB and MSTID are comparable (Figure 4 vs. Figure 7). As far as we know, the main application of ROTI is used to verify the ionospheric irregularities and scintillations at high and low latitudes (Cherniak et al., 2018; Pi et al.,
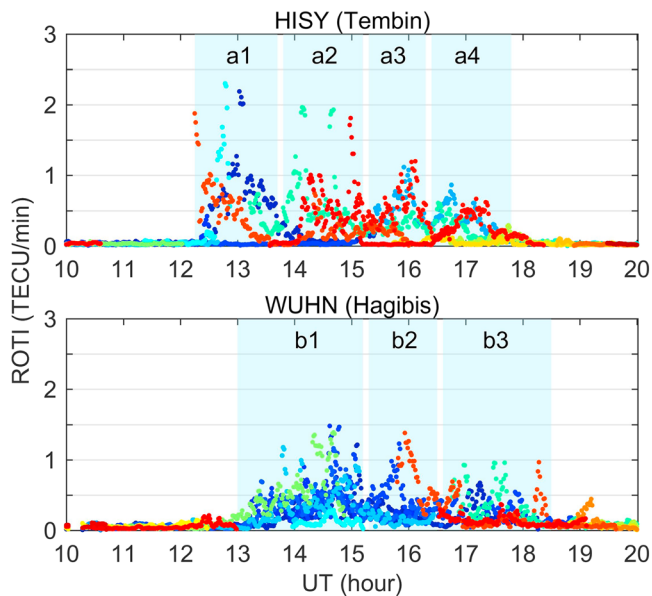
Figure 12. Time series of ROTI responding to EPB (top panel) and MSTID (bottom panel) associated with Tembin on 26 August 2012 and Hagibis on 15 June 2014, respectively. ROTI = rate of total electron content index; TECU = total electron content unit.

1997). The positive correlation between ROTI and scintillation indexes S_4 and σ_φ were also confirmed by many studies (e.g., Luo et al., 2018; Pi et al., 2013; Yang & Liu, 2016b). Figures 4 and 7 indicate that the ROTI is sensitive to both plasma bubble and MSTID, suggesting that cautions should be taken when ROTI maps are used to identify the ionospheric irregularities. We also noted that the ROTI maps have been applied in determining the bubbles within 20–45 °N and 80–110 °E in China during the magnetic storm on 8 September 2017 (Aa et al., 2018). It is strongly suggested that researchers should take multi-instrument such as iono-sonde or ISMR to do the cross validation rather than only relying on ROTI maps.

Figure 12 presents two typical ROTI variations responding to plasma bubble and MSTID. Different color represents different GPS satellite (see the color bar in Figure 5). The ROTIs are derived from GPS stations HISY and WUHN, respectively. These two stations are selected since they are very close to the ionosonde stations, which can be used to do the cross validation (see Figures 5 and 8). To analyze the difference of ROTI variations responding to plasma bubble and MSTID, several fluctuation events are confirmed in Figure 12. The classification of a fluctuation event is satisfied: (a) ROTI values for one satellite have to remain above the threshold value of 0.5 TECU/min for a minimum period of 10 min and (b) at least two satellites show ROTI perturbation during this minimum period. According to this classification, four obvious fluctuations of ROTI marked with "a1," "a2," "a3," and "a4" can be seen in the top panel of Figure 12 during 12:00–18:00 UT. That means the radio wave signals of GPS satellites have to propagate through at least four small-scale (Fresnel scale) irregularities in the bubble, thus resulting in signal diffractive effects (Kintner et al., 2007). Under this condition, the ionospheric scintillations are generated as shown in Figure 4 of Yang and Liu (2016a). Different from the plasma bubble, the time series of ROTI responding to MSTID show a relatively slow fluctuation with small magnitude (ROTI < 1.5 TECU/min) marked with "b1," "b2," and "b3," indicating that the large scale of MSTID mainly results in positive or negative TEC disturbances as shown in Figures 2 and 4 in Song et al. (2017). This result is also consistent with the absence of spread-F over WHZL station (near WUHN station) in Figure 9.

The characteristics of EPB and MSTID related to Tembin and Hagibis are analyzed in detail in this study based on multi-instrumental observations. Several possibilities may cause the different ionospheric responses during the lifetimes of tropical cyclones. An obvious difference between the two tropical cyclones is their intensity. According to the Hong Kong Observatory (2012, 2014), the v_{max} of Tembin on 26 August 2012 can reach 41 m/s (typhoon level), while that of Hagibis on 15 June 2014 was only 21 m/s (tropical storm level). Polyakova and Perevalova (2011) investigated the ionospheric disturbances when three tropical cyclones were close to the U.S. Atlantic coast during August–October 2005 and revealed an increase in TEC variations when tropical cyclones reached their peak intensity, but the magnitudes of TEC variations were not directly correlated with the intensity of three cyclones. Focusing on the Far East region, the night-time anomalies in the lower ionosphere induced by six tropical cyclone events have been shown in Rozhnoi et al. (2014). They did not find any direct correlation between the tropical cyclone intensity and magnitude of the signal anomalies in the ionosphere as well. The latest finding in Ke et al. (2019) also pointed out that the intensity of scintillation caused by EPBs was not correlated to the wind velocity of tropical cyclone center based on correlation analysis. From the above discussions, we think that the different ionospheric irregularities shown in this study should not be related to the intensity of two tropical cyclones.

Another difference between two cyclones is their occurrence season. In the Northern Hemisphere, the tropical cyclone Tembin occurred during 18–30 August 2012, which is close to autumn equinox, while that of Hagibis took place during summer solstice. It is well known that at low-latitude of East-Asia postsunset EPBs have higher occurrence rate in autumn/spring equinox rather than in summer/winter solstice (e.g., Burke et al., 2004; Liu et al., 2015; Stolle et al., 2006; Xiong et al., 2010). The seasonal dependence of EPBs at a
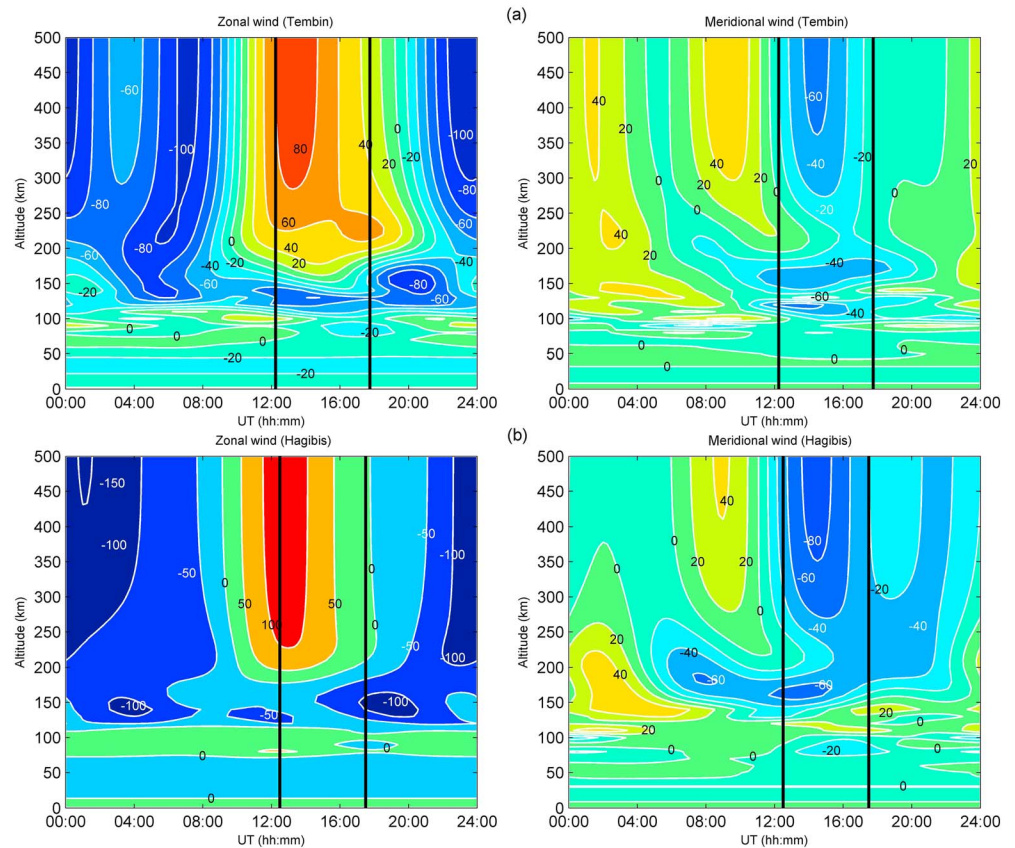
Figure 13. Temporal variations of zonal and meridional wind fields (positive eastward and northward) from the Horizontal Wind Model 2007 for the tropical cyclone Tembin on 26 August 2012 (a) and Hagibis on 15 June 2014 (b) from 0 to 500 km. The vertical black solid lines represent the perturbations time of plasma bubble and MSTID associated with Tembin and Hagibis, respectively.

given longitude is controlled by the magnetic declination and geographic latitude of the dip equator. At East-Asia longitudes, the declination of the geomagnetic field is almost equal to zero during equinoxes (Otsuka, 2018; Tsunoda, 1985). Tsunoda (1985) proposed that the occurrence frequencies of postsunset plasma bubbles can reach the peak when the solar terminator (dependent on season) is nearly parallel to the geomagnetic meridian (dependent on longitude). Based on this point, the EPB occurred on 26 August near autumn equinox of 2012 is reasonable. However, the initial seed responsible for this EPB production is not clear yet. As mentioned before, the gravity wave can drive the Rayleigh-Taylor instability and then lead to EPBs occurrence, but this source is generally triggered when the tropical cyclone is landing or near a mainland coast (e.g., Xiao et al., 2007). From Figure 3a, we can see that the Tembin on August 26 did not land the mainland of China, but on this day, it was rightly under the influence of another super typhoon Bolaven (v_{max} = 52 m/s) over the western North Pacific and turned to move east-northeastward on 27 August according to the Hong Kong Observatory in 2012 (Hong Kong Observatory, 2012). Under the interaction of Bolaven on August 26, the v_{max} of Tembin at 12:00–18:00 UT (EPB occurrence) was decreased from 41 to 39 m/s, so we presume that the gravity wave might be induced by the rapidly loss of momentum from two cyclones interaction. Different from the EPB occurred near autumn equinox, the nighttime MSTID associated with Hagibis was rightly observed in East-Asia summer. Around summer solstice in East-Asia sector, frequent nighttime MSTIDs activities related to the Perkins instability (Perkins, 1973) have been reported before (e.g., Otsuka et al., 2011; Shiokawa et al., 2003, 2005). According to the model of Perkins instability, the growth rate of this instability is inversely proportional to the neutral air density (Kotake et al., 2007; Perkins, 1973), and the density in the thermosphere shows a minimum during summer solstice (Moore & Boulton, 1987). That is why frequent nighttime MSTIDs attributed to the Perkins instability occurred in

East-Asia summer (Ding et al., 2011). However, the Perkins instability needs other mechanisms such as gravity wave seeding (Kelley & Fukao, 1991) and sporadic E layer instability (Cosgrove & Tsunoda, 2002) to reinforce it and finally trigger MSTIDs occurrence. Under this condition, the gravity wave associated with the tropical cyclone Hagibis has the possibility to enhance the growth rate of Perkins instability. In addition, the sporadic E layers with frequencies between 2 and 8 MHz during 13:30–15:30 UT on 15 June 2014 can be seen in Figure 9. The coupling process between the sporadic E and F layers may also play an important factor to induce the MSTID occurrence shown in our study. The similar speculation can also be seen in the latest research (e.g., Song et al., 2019). Based on the above discussions, we think that the occurrence seasons of two tropical cyclones should play an important role for the difference of two ionospheric irregularities.

In addition, we also investigated the background wind fields during Tembin and Hagibis. Figure 13 shows the temporal variations of zonal (left panels) and meridional (right panels) winds for the Tembin on 26 August 2012 and Hagibis on 15 June 2014 from 0 to 500 km. The vertical black solid lines represent the perturbations time of plasma bubble (12:15–17:45 UT) and MSTID (12:30–17:30 UT). The background wind fields are derived from the Horizontal Wind Model 2007 empirical model (Drob et al., 2008). As shown in Figure 13, the zonal/meridional winds were basically eastward/southward during the perturbations time regardless of plasma bubble associated with Tembin or MSTID related to Hagibis. Meanwhile, the magnitudes of winds speed during two tropical cyclones were also comparable in ionosphere $F2$ region around 12:30 UT when ionospheric irregularities began to occur. In addition, according to the background wind-filtering theory, the horizontal direction of the MSTID associated with Hagibis should be northwestward rather than the southwestward propagation as shown in Figures 7 and 8. This inconsistency can be also seen in Song et al. (2017). Based on wind predictions from the empirical model, we think that the background winds have small probability to result in the difference of two ionospheric irregularities in this study. The detailed causes, such as the seeding and the propagation of gravity wave, as well as the influence on the background atmosphere/ionosphere need further investigation.

5. Summary

In this work, we present the detailed analysis of ionospheric irregularities responding to tropical cyclones using multi-instrumental observations including those from GPS satellites, ionosondes, and Swarm satellites. The main findings are summarized as follows:

1. The plasma bubble observed on 26 August 2012 during the passage of the tropical cyclone Tembin was neither drifted from its west nor formed locally but initiated from the magnetically equatorial region.
2. The MSTID detected on 15 June 2014 when the tropical cyclone Hagibis was near the mainland coast was verified with a southwestward propagation at a mean horizontal velocity of 156 m/s.
3. The ROTI maps are sensitive to both plasma bubble and MSTID, indicating cautions should be taken when the ROTI maps are used to identify ionospheric irregularities. It is strongly suggested that researchers should take multi-instrument such as ionosonde or ISMR to do the cross validation of irregularities rather than only relying on ROTI maps.
4. By comparing the ionospheric observations during the two cyclones, we find that small-scale irregularities associated with plasma bubble cause obvious perturbations of the ROTIs with the value of ~3.0 TECU/min; while the MSTID in midlatitude causes relatively slight ROTI disturbances with the value of ~1.5 TECU/min.
5. Similar to EPB, the MSTID observed in this study also shows the feature of magnetic conjugacy based on ROTI and Ne observations. However, the ROTI and Ne in the Southern Hemisphere were much smaller than those in the Northern Hemisphere (0.3 vs. 1.5 TECU/min for ROTI; 0.8×10^{11} m^{-3} vs. 5.0×10^{11} m^{-3} for Ne). These discrepancies of ROTI and Ne between two hemispheres are likely to be caused by the seasonal influence on the background ionosphere.

References

Aa, E., Huang, W., Liu, S., Ridley, A., Zou, S., Shi, L., et al. (2018). Midlatitude plasma bubbles over China and adjacent areas during a magnetic storm on 8 September 2017. *Space Weather*, *16*, 321–331. https://doi.org/10.1002/2017SW001776
Abdu, M. A., Kherani, E., Batista, I. S., de Paula, E., Fritts, D. C., & Sobral, J. H. A. (2009). Gravity wave initiation of equatorial spread F/plasma bubble irregularities based on observational data from the SpreadFEx campaign. *Annales Geophysicae*, *27*(7), 2607–2622. https://doi.org/10.5194/angeo-27-2607-2009

Appleton, E. V. (1946). Two anomalies in the ionosphere. *Nature*, *157*(3995), 691. https://doi.org/10.1038/157691a0

Burke, W. J., Gentile, L. C., Huang, C. Y., Valladares, C. E., & Su, S. Y. (2004). Longitudinal variability of equatorial plasma bubbles observed by DMSP and ROCSAT-1. *Journal of Geophysical Research*, *109*, A12301. https://doi.org/10.1029/2004JA010583

Cherniak, I., Krankowski, A., & Zakharenkova, I. (2018). ROTI Maps: A new IGS's ionospheric product characterizing the ionospheric irregularities occurrence. *GPS Solutions*, *22*(3), 1–12. https://doi.org/10.1007/s10291-018-0730-1

Chou, M. Y., Lin, C. C. H., Yue, J., Tsai, H. F., Sun, Y. Y., Liu, J. Y., & Chen, C. H. (2017). Concentric traveling ionosphere disturbances triggered by Super Typhoon Meranti (2016). *Geophysical Research Letters*, *44*, 1219–1226. https://doi.org/10.1002/2016GL072205

Cosgrove, R. B., & Tsunoda, R. T. (2002). A direction-dependent instability of sporadic-*E* layers in the nighttime midlatitude ionosphere. *Geophysical Research Letters*, *29*(18), 1864. https://doi.org/10.1029/2002GL014669

de Paula, E. R., Muella, M. T. A. H., Sobral, J. H. A., Abdu, M. A., Batista, I. S., Beach, T. L., & Groves, K. M. (2010). Magnetic conjugate point observations of kilometer and hundred-meter scale irregularities and zonal drifts. *Journal of Geophysical Research*, *115*, A08307. https://doi.org/10.1029/2010JA015383

Dhaka, S. K., Takahashi, M., Shibagaki, Y., Yamanaka, M. D., & Fukao, S. (2003). Gravity wave generation in the lower stratosphere due to passage of the typhoon 9426 (Orchid) observed by the MU radar at Shigaraki (34.85 °N, 136.10 °E). *Journal of Geophysical Research*, *108*(D19), 4595. https://doi.org/10.1029/2003JD003489

Ding, F., Wan, W., Xu, G., Yu, T., Yang, G., & Wang, J. (2011). Climatology of medium-scale traveling ionospheric disturbances observed by a GPS network in central China. *Journal of Geophysical Research*, *116*, A09327. https://doi.org/10.1029/2011JA016545

Drob, D. P., Emmert, J. T., Crowley, G., Picone, J. M., Shepherd, G. G., Skinner, W., et al. (2008). An empirical model of the Earth's horizontal wind fields: HWM07. *Journal of Geophysical Research*, *113*, A12304. https://doi.org/10.1029/2008JA013668

Fritts, D. C., Vadas, S. L., Riggin, D. M., Abdu, M. A., Batista, I. S., Takahashi, H., et al. (2008). Gravity wave and tidal influences on equatorial spread F based on observations during the spread F Experiment (SpreadFEx). *Annales Geophysicae*, *26*(11), 3235–3252. https://doi.org/10.5194/angeo-26-3235-2008

Hernández-Pajares, M., Juan, J. M., & Sanz, J. (2006). Medium-scale traveling ionospheric disturbances affecting GPS measurements: Spatial and temporal analysis. *Journal of Geophysical Research*, *111*, A07S11. https://doi.org/10.1029/2005JA011474

Hong Kong Observatory (2012). *Tropical cyclones in 2012*. Hong Kong. [Available at: Hong Kong Observatory. http://www.hko.gov.hk/publica/tc/TC2012.pdf

Hong Kong Observatory (2014). *Tropical cyclones in 2014*. Hong Kong. [Available at: Hong Kong Observatory. http://www.hko.gov.hk/publica/tc/TC2014.pdf

Huang, C. S., & Kelley, M. C. (1996). Nonlinear evolution of equatorial spread F, 1. On the role of plasma instabilities and spatial resonance associated with gravity wave seeding. *Journal of Geophysical Research*, *101*(A1), 283–292. https://doi.org/10.1029/95JA02211

Huang, Y. N., Cheng, K., & Chen, S. W. (1985). On the detection of acoustic-gravity waves generated by typhoon by use of real time HF Doppler frequency shift sounding system. *Radio Science*, *20*(4), 897–906. https://doi.org/10.1029/RS020i004p00897

Isaev, N. V., Kostin, V. M., Belyaev, G. G., Ovcharenko, O. Y., & Trushkina, E. P. (2010). Disturbances of the topside ionosphere caused by typhoons. *Geomagnetism Aeronomy*, *50*(2), 243–255. https://doi.org/10.1134/S001679321002012X

Ke, F., Wang, J., Tu, M., Wang, X., Zhao, X., & Deng, J. (2018). Morphological characteristics and coupling mechanism of the ionospheric disturbance caused by Super Typhoon Sarika in 2016. *Advances in Space Research*, *62*(5), 1137–1145. https://doi.org/10.1016/j.asr.2018.06.015

Ke, F., Wang, J., Tu, M., Wang, X., Wang, X., Zhao, X., & Deng, J. (2019). Characteristics and coupling mechanism of GPS ionospheric scintillation responses to the tropical cyclones in Australia. *GPS Solutions*, *23*(2), 1–14. https://doi.org/10.1007/s10291-019-0826-2

Kelley, M. C. (2009). *The Earth's ionosphere: Plasma physics and electrodynamics* (2nd ed.). New Work: Elsevier.

Kelley, M. C., & Fukao, S. (1991). Turbulent upwelling of the mid-latitude ionosphere, 2. Theoretical framework. *Journal of Geophysical Research*, *96*(A3), 3747–3753. https://doi.org/10.1029/90JA02252

Kim, H., Kim, J., Ho, C., & Chu, P. (2010). Pattern classification of typhoon tracks using the fuzzy c-means clustering method. *Journal of Climate*, *24*(2), 488–508. https://doi.org/10.1175/2010JCLI3751.1

Kim, S., & Chun, H. (2005). A numerical study of gravity waves induced by convection associated with Typhoon Rusa. *Geophysical Research Letters*, *32*, L24816. https://doi.org/10.1029/2005GL024662

Kim, S., & Chun, H. (2011). Impact of typhoon-generated gravity waves in the typhoon development. *Geophysical Research Letters*, *38*, L01806. https://doi.org/10.1029/2010GL045719

Kim, S., Chun, H., & Wu, D. L. (2009). A study on stratospheric gravity waves generated by Typhoon Ewiniar: Numerical simulations and satellite observations. *Journal of Geophysical Research*, *114*, D22104. https://doi.org/10.1029/2009JD011971

Kintner, P. M., Ledvina, B. M., & de Paula, E. R. (2007). GPS and ionospheric scintillations. *Space Weather*, *5*, S09003. https://doi.org/10.1029/2006SW000260

Kong, J., Yao, Y., Xu, Y., Kuo, C., Zhang, L., Liu, L., & Zhai, C. (2017). A clear link connecting the troposphere and ionosphere: Ionospheric responses to the 2015 Typhoon Dujuan. *Journal of Geodesy*, *91*(9), 1087–1097. https://doi.org/10.1007/s00190-017-1011-4

Kotake, N., Otsuka, Y., Ogawa, T., Tsugawa, T., & Saito, A. (2007). Statistical study of medium-scale traveling ionospheric disturbances observed with the GPS networks in Southern California. *Earth Planets Space*, *59*(2), 95–102. https://doi.org/10.1186/BF03352681

Lay, E. H. (2018). Ionospheric irregularities and acoustic/gravity wave activity above low-latitude thunderstorms. *Geophysical Research Letters*, *45*, 90–97. https://doi.org/10.1002/2017GL076058

Lejeune, S., Wautelet, G., & Warnant, R. (2012). Ionospheric effects on relative positioning within a dense GPS network. *GPS Solutions*, *16*(1), 105–116. https://doi.org/10.1007/s10291-011-0212-1

Li, W., Yue, J., Wu, S., Yang, Y., Li, Z., Bi, J., & Zhang, K. (2018). Ionospheric responses to typhoons in Australia during 2005–2014 using GNSS and FORMOSAT-3/COSMIC measurements. *GPS Solutions*, *22*(3), 1–11. https://doi.org/10.1007/s10291-018-0722-1

Lin, C. H., Liu, J. Y., Fang, T. W., Chang, P. Y., Tsai, H. F., Chen, C. H., & Hsiao, C. C. (2007). Motions of the equatorial ionization anomaly crests imaged by FORMOSAT-3/COSMIC. *Geophysical Research Letters*, *34*, L19101. https://doi.org/10.1029/2007GL030741

Liu, K., Li, G., Ning, B., Hu, L., & Li, H. (2015). Statistical characteristics of low-latitude ionospheric scintillation over China. *Advances in Space Research*, *55*(5), 1356–1365. https://doi.org/10.1016/j.asr.2014.12.001

Liu, L., Zhao, B., Wan, W., Venkartraman, S., Zhang, M., & Yue, X. (2007). Yearly variations of global plasma densities in the topside ionosphere at middle and low latitudes. *Journal of Geophysical Research*, *112*, A07303. https://doi.org/10.1029/2007JA012283

Luo, X., Lou, Y., Xiao, Q., Gu, S., Chen, B., & Liu, Z. (2018). Investigation of ionospheric scintillation effects on BDS precise point positioning at low-latitude regions. *GPS Solutions*, *22*(3), 1–12. https://doi.org/10.1007/s10291-018-0728-8

Luo, X., Xiong, C., Gu, S., Lou, Y., Stolle, C., Wan, X., et al. (2019). Geomagnetically conjugate observations of equatorial plasma irregularities from Swarm constellation and ground-based GPS stations. *Journal of Geophysical Research: Space Physics*, 124, 3650–3665. https://doi.org/10.1029/2019JA026515

Moore, P., & Boulton, W. J. (1987). Some aspects of a global thermospheric density model deduced from the analysis of the orbit of Intercosmos 13 rocket (1975–22B). *Planetary and Space Science*, 35(8), 1039–1052. https://doi.org/10.1016/0032-0633(87)90008-0

Otsuka, Y. (2018). Review of the generation mechanisms of post-midnight irregularities in the equatorial and low-latitude ionosphere. *Progress in Earth and Planetary Science*, 5(1), 1–13. https://doi.org/10.1186/s40645-018-0212-7

Otsuka, Y., Kotake, N., Shiokawa, K., Ogawa, T., Tsugawa, T., & Saito, A. (2011). Statistical study of medium-scale traveling ionospheric disturbances observed with a GPS receiver network in Japan. In M. Abdu, & D. Pancheva (Eds.), *Aeronomy of the Earth's Atmosphere and Ionosphere*, IAGA Special Sopron Book Series (Vol. 2, pp. 291–299). Dordrecht: Springer. https://doi.org/10.1007/978-94-007-0326-1_21

Perkins, F. (1973). Spread F and ionospheric currents. *Journal of Geophysical Research*, 78(1), 218–226. https://doi.org/10.1029/JA078i001p00218

Pi, X., Mannucci, A. J., Lindqwister, U. J., & Ho, C. M. (1997). Monitoring of global ionospheric irregularities using the worldwide GPS network. *Geophysical Research Letters*, 24(18), 2283–2286. https://doi.org/10.1029/97GL02273

Pi, X., Mannucci, A. J., Valant-spaight, B., Bar-sever, Y., Romans, L. J., Skone, S., et al. (2013). Observations of global and regional ionospheric irregularities and scintillation using GNSS tracking networks. Proc. ION 2013 Pacific PNT Meeting, Institute of Navigation, Honolulu, Hawaii, April 23–25 (pp. 752–761).

Polyakova, A. S., & Perevalova, N. P. (2011). Investigation into impact of tropical cyclones on the ionosphere using GPS sounding and NCEP/NCAR Reanalysis data. *Advances in Space Research*, 48(7), 1196–1210. https://doi.org/10.1016/j.asr.2011.06.014

Rivoire, L., Birner, T., & Knaff, J. A. (2016). Evolution of the upper-level thermal structure in tropical cyclones. *Geophysical Research Letters*, 43, 10,530–10,537. https://doi.org/10.1002/2016GL070622

Rozhnoi, A., Solovieva, M., Levin, B., Hayakawa, M., & Fedun, V. (2014). Meteorological effects in the lower ionosphere as based on VLF/LF signal observations. *Natural Hazards and Earth System Sciences*, 14(10), 2671–2679. https://doi.org/10.5194/nhess-14-2671-2014

Saito, A., Iyemori, T., Blomberg, L. G., Yamamoto, M., & Takeda, M. (1998). Conjugate observations of the mid-latitude electric field fluctuations with the MU radar and the Freja satellite. *Journal of Atmospheric and Solar-Terrestrial Physics*, 60(1), 129–140. https://doi.org/10.1016/S1364-6826(97)00094-1

Shiokawa, K., Ihara, C., Otsuka, Y., & Ogawa, T. (2003). Statistical study of nighttime medium-scale traveling ionospheric disturbances using midlatitude airglow images. *Journal of Geophysical Research*, 108(A1), 1052. https://doi.org/10.1029/2002JA009491

Shiokawa, K., Otsuka, Y., Tsugawa, T., Ogawa, T., Saito, A., Ohshima, K., et al. (2005). Geomagnetic conjugate observation of nighttime medium-scale and large-scale traveling ionospheric disturbances: FRONT3 campaign. *Journal of Geophysical Research*, 110, A05303. https://doi.org/10.1029/2004JA010845

Singh, S., Johnson, F. S., & Power, R. A. (1997). Gravity wave seeding of equatorial plasma bubbles. *Journal of Geophysical Research*, 102(A4), 7399–7410. https://doi.org/10.1029/96JA03998

Song, Q., Ding, F., Zhang, X., Liu, H., Mao, T., Zhao, X., & Wang, Y. (2019). Medium-scale traveling ionospheric disturbances induced by typhoon Chan-hom over China. *Journal of Geophysical Research: Space Physics*, 124, 2223–2237. https://doi.org/10.1029/2018JA026152

Song, Q., Ding, F., Zhang, X., & Mao, T. (2017). GPS detection of the ionospheric disturbances over China due to impacts of Typhoons Rammasum and Matmo. *Journal of Geophysical Research: Space Physics*, 122, 1055–1063. https://doi.org/10.1002/2016JA023449

Sorokin, V. M., Isaev, N. V., Yaschenko, A. K., Chmyrev, V. M., & Hayakawa, M. (2005). Strong DC electric field formation in the low latitude ionosphere over typhoons. *Journal of Atmospheric and Solar-Terrestrial Physics*, 67(14), 1269–1279. https://doi.org/10.1016/j.jastp.2005.06.014

Stolle, C., Lu, H., Rother, M., & Balasis, G. (2006). Magnetic signatures of equatorial spread F as observed by the CHAMP satellite. *Journal of Geophysical Research*, 111, A02304. https://doi.org/10.1029/2005JA011184

Takahashi, H., Taylor, M. J., Pautet, P. D., Medeiros, A. F., Gobbi, D., Wrasse, C. M., et al. (2009). Simultaneous observation of ionospheric plasma bubbles and mesospheric gravity waves during the SpreadFEx Campaign. *Annales Geophysicae*, 27(4), 1477–1487. https://doi.org/10.5194/angeo-27-1477-2009

Taori, A., Patra, A. K., & Joshi, L. M. (2011). Gravity wave seeding of equatorial plasma bubbles: An investigation with simultaneous *F* region, *E* region, and middle atmospheric measurements. *Journal of Geophysical Research*, 116, A05310. https://doi.org/10.1029/2010JA016229

Tsugawa, T., Otsuka, Y., Coster, A. J., & Saito, A. (2007). Medium-scale traveling ionospheric disturbances detected with dense and wide TEC maps over North America. *Geophysical Research Letters*, 34, L22101. https://doi.org/10.1029/2007GL031663

Tsunoda, P. T. (1985). Control of the seasonal and longitudinal occurrence of equatorial scintillations by the longitudinal gradient in integrated *E* region Pedersen conductivity. *Journal of Geophysical Research*, 90(A1), 447–456. https://doi.org/10.1029/JA090iA01p00447

Valladares, C. E., & Sheehan, R. (2016). Observations of conjugate MSTIDs using networks of GPS receivers in the American sector. *Radio Science*, 51, 1470–1488. https://doi.org/10.1002/2016RS005967.Received

Xiao, Z., Xiao, S., Hao, Y., & Zhang, D. (2007). Morphological features of ionospheric response to typhoon. *Journal of Geophysical Research*, 112, A04304. https://doi.org/10.1029/2006JA011671

Xiong, C., Park, J., Lühr, H., Stolle, C., & Ma, S. Y. (2010). Comparing plasma bubble occurrence rates at CHAMP and GRACE altitudes during high and low solar activity. *Annales Geophysicae*, 28(9), 1647–1658. https://doi.org/10.5194/angeo-28-1647-2010

Yang, Z., & Liu, Z. (2016a). Observational study of ionospheric irregularities and GPS scintillations associated with the 2012 tropical cyclone Tembin passing Hong Kong. *Journal of Geophysical Research: Space Physics*, 121, 4705–4717. https://doi.org/10.1002/2016JA022398.Received

Yang, Z., & Liu, Z. (2016b). Correlation between ROTI and ionospheric scintillation indices using Hong Kong low-latitude GPS data. *GPS Solutions*, 20(4), 815–824. https://doi.org/10.1007/s10291-015-0492-y

Zakharenkova, I., Astafyeva, E., & Cherniak, I. (2016). GPS and in situ Swarm observations of the equatorial plasma density irregularities in the topside ionosphere. *Earth, Planets and Space*, 68(1), 1–11. https://doi.org/10.1186/s40623-016-0490-5

Zakharov, V. I., & Kunitsyn, V. E. (2012). Regional features of atmospheric manifestations of tropical cyclones according to ground based GPS network data. *Geomagnetism Aeronomy*, 52(4), 533–545. https://doi.org/10.1134/S0016793212040160